Evolution of Interphase and Intergranular Stresses in Zr-2.5Nb During Room Temperature Deformation

Cai, S.; Daymond, M.R.; Holt, R.A.; Gharghouri, M.A.; Oliver, E.C.

Publisher's version / Version de l'éditeur:
https://doi.org/10.1016/j.msea.2008.10.016
Materials Science and Engineering A, 501, pp. 166-181, 2009

Materials Science and Engineering A 501 (2009) 166–181

Contents lists available at ScienceDirect

Materials Science and Engineering A

journal homepage: www.elsevier.com/locate/msea

Evolution of interphase and intergranular stresses in Zr–2.5Nb during room temperature deformation

S. Cai[a], M.R. Daymond[a,*], R.A. Holt[a], M.A. Gharghouri[b], E.C. Oliver[c]

[a] Dept. of Mechanical and Materials Engineering, Queen's University, Nicol Hall, 60 Union Street, Kingston, Canada K7L 3N6
[b] NRC, Canadian Neutron Beam Centre, Chalk River, ON K0J 1J0, Canada
[c] ISIS, Rutherford Appleton Lab., Didcot, OX11 0QX, UK

ARTICLE INFO

Article history:
Received 18 August 2008
Received in revised form
23 September 2008
Accepted 8 October 2008

Keywords:
Interphase
Intergranular strain
Neutron diffraction
Asymmetric yielding
Strength differential
Zr–2.5Nb

ABSTRACT

Both *in situ* tension and compression tests have been carried out on textured Zr–2.5Nb plate material at room temperature. Deformation along all the three principle plate directions has been studied and the evolution of interphase and intergranular strains along the loading and the principle Poisson's directions has been investigated by neutron diffraction. The evolution of interphase and intergranular strain was determined by the relative phase properties, crystal properties and texture distribution. The average phase behaviors are similar during tension and compression, where the β-phase in this material is stronger than the α-phase. The asymmetric yielding of the α-{0 0 0 2} grain family results in a relatively large intergranular strain in the loading direction during compression and different dependence of strength during tension and compression on texture. The combination of the thermal residual stress and the asymmetric CRSS in the ⟨*c*⟩ axis gives the {0 0 0 2} grain family a higher strength in compression than in tension.

1. Introduction

Due to its good mechanical strength, high corrosion resistance and strong creep resistance, combined with excellent neutronic properties, Zr–2.5 wt.% Nb has been selected as the pressure tube material for CANDU reactors since the 1970s [1]. Its in-reactor properties such as hydride cracking, irradiation growth and creep have been of interest for decades and models have been established to simulate the irradiation behavior [2–6]. It has been found that the irradiation behavior of Zr–2.5Nb pressure tubes is strongly dependent on the texture, microstructure and intergranular residual stresses [7–10], which are controlled by the manufacturing schedule. The general fabrication route of CANDU pressure tubes consists of extrusion at ~800 °C, air cooling, cold draw to ~20–30% strain and autoclaving at 400 °C for 24 h. After extrusion, it consists of ~90% *hcp* α-Zr, which has Nb content <1%, and ~10% metastable *bcc* β-Zr, which contains approximately 20% Nb. During autoclaving, β-Zr partially transforms to β-Nb (~95% Nb) and contains the metastable ω-phase and the enriched β-Zr (~50% Nb) [11]. The texture of pressure tube was found to be determined at the extrusion stage and not changed during subsequent cold working [12]. At lower extrusion temperatures, the texture of the α-phase is controlled by dislocation slip, while at temperatures above 700 °C other mechanisms may play a role. For example, the α-phase may inherit the texture from the β-phase by the Burgers relationship during transformation or be reoriented by body rotation and phase boundary sliding [12,13]. Annealing at temperatures below the β-transus temperature usually does not produce the recrystallization texture observed in single phase Zirconium [14]. Recently, a new processing schedule was used in India where the cold drawing and autoclaving were replaced by two stage cold pilgering process with an intermediate annealing (550 °C, 6 h) and the final annealing (400 °C, 72 h). The deformation strain is ~60% in the first stage cold working and ~25% in the second stage cold working [15]. Still, no significant texture development in the α-phase occurs during cold working and no recrystallization is observed after the intermediate and final annealing [16]. Kumar et al. [17] proposed that at room temperature the β-phase is relatively softer than the α-phase and thus the plastic flow is mainly confined to the β-matrix, restricting the texture change in the α-phase. However, our work suggests that the β-phase is actually stronger than the α-phase and yields at a higher macroscopically applied stress during uniaxial deformation [18].

Investigations on deformation of Zr–2.5Nb pressure tube material by other authors revealed that the texture evolution during cold work is the result of the competition between dislocation slip and

* Corresponding author. Tel.: +1 613 533 2193; fax: +1 613 533 6610.
E-mail address: daymond@me.queensu.ca (M.R. Daymond).

0921-5093/$ – see front matter © 2008 Elsevier B.V. All rights reserved.
doi:10.1016/j.msea.2008.10.016

twinning [19,20]; twinning occurs preferentially in coarse grains and produces a sharp texture change during deformation, while prismatic, basal and pyramidal $\langle c+a \rangle$ slip are responsible for the texture evolution in fine grain structures. Cheadle et al. [21] tested Zr–2.5Nb in tension along a specimen direction with a high concentration of basal plane normals, but did not observe any texture change associated with twinning for plastic strains less than 10%. Kim's study [22] of an annealed Zr–2.5Nb pressure tube material, which has an equiaxed grain structure with size of ~10 μm, shows that deformation twinning occurred only after strains greater than 5%. Twinning is thus not likely to be operating in the early stage of deformation where strain is less than 5% [23]. Despite the lack of twinning, Zr–2.5Nb pressure tube material yields anisotropically, and attempts to model the anisotropic mechanical behavior by a power law constitutive model or a polycrystalline model [23,24] have not been very successful.

Part of the reason for the lack progress in modeling the behavior of this material is that much of the previous work focused on the irradiation behavior such as creep and growth, while the short term deformation mechanisms of Zr–2.5Nb such as the relative contribution of each phase, the interactions between different deformation systems and the evolution of interphase and intergranular stress–strain during deformation has not been thoroughly studied. Even the studies of irradiation induced deformation were restricted to pressure tube material with a limited range of microstructures and texture, where the basal plane normals are distributed in the radial and transverse plane and, mostly, concentrated in the transverse direction [25]. The models developed were accurate over only a narrow range of textures and microstructure and could not be accurately extrapolated to textures quite different from that of these pressure tubes. This has significantly restricted the understanding of the relationship of texture and microstructure to irradiation growth and creep. To the authors' knowledge, a deformation model which can be used and applied directly to such a material taking into account the anisotropy and the dual phase nature has not yet been constructed. Indeed, most of the studies to date have ignored the β-phase because of its relatively small volume fraction and have treated the material as single phase polycrystalline [3,4,23,26] with the aim of accommodating any related error within the fit of the parameters of the single phase models to the experimental data. However, recent studies [27] have suggested that the overall properties of Zr–2.5Nb may be highly dependent on the properties and the distribution (both geometric and texture) of the β-phase. Neglecting the β-phase is thus likely to introduce significant errors in modeling the deformation response of the overall material and in particular in extrapolating model predictions to new textures and microstructures. This is one likely reason why the models in [3] and [4] are accurate only for certain texture and microstructure combinations.

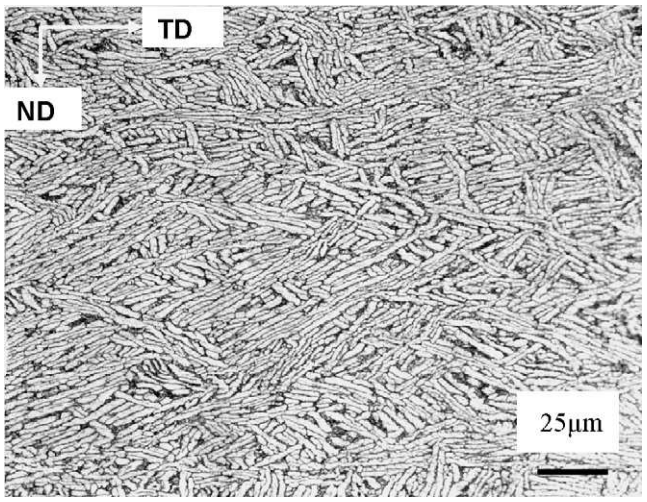

Fig. 1. Microstructure of hot rolled Zr–2.5Nb showing elongated α-phase grains (light) surrounded by β-phase (dark).

This paper presents our recent study on the deformation behavior of a hot rolled Zr–2.5Nb plate material at room temperature. Both tension and compression tests were carried out along three principal plate directions, while neutron diffraction was employed to monitor the evolution of interphase and intergranular strains along the loading and two Poisson directions. A large data set has been collected to help us to understand the fundamental deformation mechanism such as slip and twinning of this material. In addition the data base will be used to evaluate and improve current

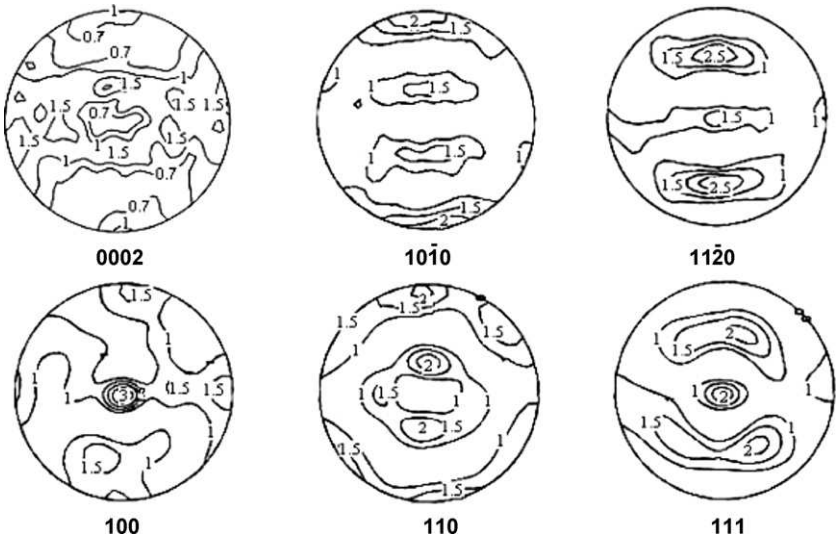

Fig. 2. Texture of hot rolled Zr–2.5Nb plate. The upper part shows the selected pole figures of the α-phase, the lower part shows the selected pole figures of the β-phase. The ND is in the center of the pole figure, the RD is vertical and TD is horizontal.

modeling approaches. We present here the experimental results of the mechanical behavior in both macroscopic and microscopic scales from which the texture dependence and the influence of the β-phase can be shown.

2. Materials and experimental method

The composition of the experimental material is 2.5 wt.% Nb, ~1200 ppm O, ~950 ppm Fe, ~110 ppm C and balance Zr. Ingots were forged to 112 mm thick at 1065 °C and then hot rolled to 56 mm thick at about 700 °C followed by a furnace cool. The microstructure at room temperature is shown in Fig. 1. The predominant α-grains have a plate-like shape with length and width ~30 μm and thickness ~3 μm, while the β-phase is distributed more or less continuously between the α-grains. The O is expected to be segregated to the α-phase while the Fe and Nb are expected to be mostly concentrated in the β-phase [28].

Texture measurement was carried on High-Pressure-Preferred Orientation (HIPPO) at Lujan Jr. Neutron Scattering Center, Los Alamos National Laboratory and calculated based on the generalized spherical-harmonics description of the effect of texture on reflection intensities in a Rietveld refinement program in GSAS [29]. Fig. 2 shows the texture of this material at room temperature. In the α-phase the ⟨*c*⟩ axis is mostly orientated towards TD and ND, while the ⟨1 0 $\bar{1}$ 0⟩ ⟨*a*⟩ axis is concentrated in RD. The resolved fractions of basal plane normal in rolling, transverse and normal direction (f_R, f_T and f_N) are 0.27, 0.39 and 0.34 [7]. The ⟨1 0 0⟩ direction of the β-phase is slightly aligned along the three principle directions. Texture was also measured at the E3 spectrometer at the National Research Universal (NRU) reactor at the AECL Chalk River Laboratory, on additional samples cut from the plate. It is noted that although a generally consistent texture are obtained at these two facilities, there is a small difference in the intensity maxima for each pole figure. The volume fraction of the β-phase obtained from Rietveld refinement is ~12%, consistent with that expected from the nominal Nb content.

Dog-bone tensile samples (with cross-section area ~6 mm × 6 mm for the RD and TD, 15 mm × 4 mm for the ND) and cylindrical compressive samples (Ø9 mm × 20 mm) were cut from the rolled plate with the longitudinal direction parallel to the rolling direction (RD), transverse direction (TD) and the plate normal direction (ND). FE analysis demonstrated that the different sample geometries had the same (i.e. uniaxial) stress state within the measurement volume. Tension and compression tests were carried out along these three principle plate directions and lattice strain evolution in the axial and transverse directions was measured intermittently during testing by neutron diffraction. Samples are defined based on the loading direction and the diffraction collecting direction, e.g. a ND–RD sample means that the loading direction is the plate normal direction and the diffraction vector is along the rolling direction.

Tensile tests were carried out on the L3 beam line at the National Research Universal reactor at the AECL Chalk River Laboratory (CRL). The (3 3 1) diffraction peak from a germanium single crystal was used as the incident beam. The wavelength was ~2.046 Å. The beam size was defined to select the center area of the sample gauge. Samples were mounted in an Applied Test System screw-driven load frame equipped with a load cell and hydraulic grips. A series of increasing uniaxial tensile loads were applied along the axial direction and the deformation strain was measured by an extensometer mounted on the sample. At each selected stress level, the detector and the sample table were rotated together such that the diffraction peaks from plane families of interest could be collected in the desired specimen direction. By rotating the load frame out of the scattering plane, both axial (parallel to the sample axis) and transverse (normal to the sample axis) lattice strains were measured. The (1 0 $\bar{1}$ 0), (1 0 $\bar{1}$ 1), (1 0 $\bar{1}$ 2), (1 0 $\bar{2}$ 0) and (0 0 0 2) diffraction peaks of the α-phase and (1 1 0), (2 0 0) and (2 1 1) diffraction peaks of the β-phase were collected. In the elastic region, the experiment was carried out in stress control, while in the plastic region it was switched to strain control. To handle the stress drop caused by room temperature relaxation observed in the plastic regime, samples were first deformed to the desired strain and then backed off 0.025% strain to eliminate any stress relaxation during neutron data acquisition.

The compression tests were carried out on ENGIN-X at the ISIS pulsed neutron facility, Rutherford Appleton Laboratory. The loading axis is horizontal and at 45° to the incident beam. Two detector banks are set up horizontally and at angles ±90° to the incident beam, allowing simultaneous measurement of lattice strains in directions both parallel and perpendicular to the applied load [30]. More details of the instrument can be found in [31]. A series of increasing uniaxial compressive loads were applied along the axial direction to produce a final true strain of ~10%. Strain was monitored on the samples using a clip gauge. The incident beam was 8 mm high and 4 mm wide, the radial collimators in use provided a scattered beam aperture of 4 mm. Experiment was under strain control, each time the sample was deformed to desired strains and held for 30 s to allow relaxation before data acquisition. Stress–strains were the average values during the data acquisition period.

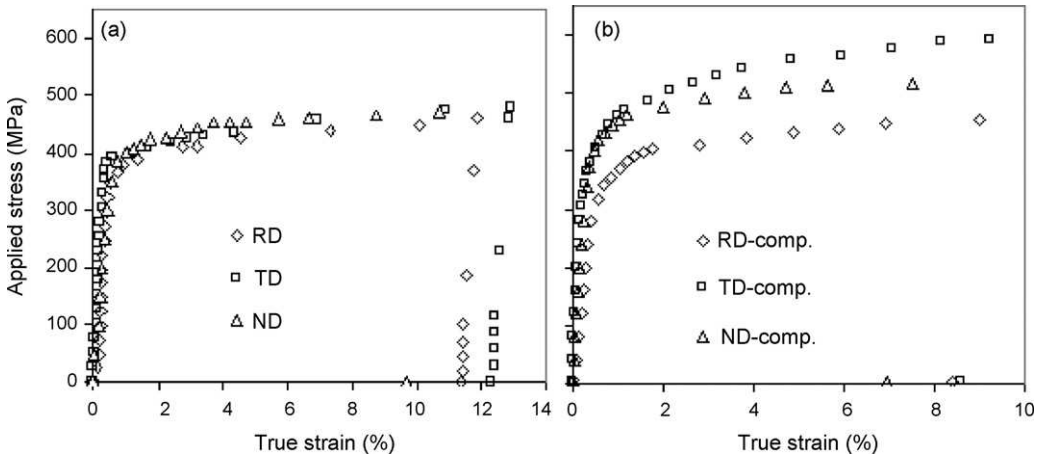

Fig. 3. Macroscopic mechanical behavior in the three principal plate directions during (a) tension and (b) compression.

Table 1
Mechanical properties in the three plate directions during tension and compression. Results are based on the average of 2–3 samples in each plate direction.

	RD		TD		ND	
	Tension	Comp.	Tension	Comp.	Tension	Comp.
E (GPa)	90.5 ± 7	84.1 ± 6.5	101 ± 5.6	105.5 ± 10.3	91 ± 11.5	100 ± 14.6
$\sigma_{0.2}$ (MPa)	370 ± 8.1	345 ± 12.9	395 ± 7	420 ± 7	385 ± 7	422.5 ± 10.6

The mechanical responses of individual grain families were easily determined by single peak fitting, while different techniques were used to estimate the average phase behavior based on the characteristics of the beam used. For tensile tests carried out at CRL where monochromatic beam is used, the average phase strain was calculated using the Method B weighting equations discussed in [32].

For compression tests carried out at ISIS where time-of-flight is employed, the average phase strains are commonly determined by a multiphase Rietveld refinement for materials with a weak to medium texture [33,34]. Due to the weak texture of this material, Rietveld refinement is employed to determine the average phase strains of the α-and β-phases. The advantage of using this approach to determine the average phase response is that it can obtain rea-

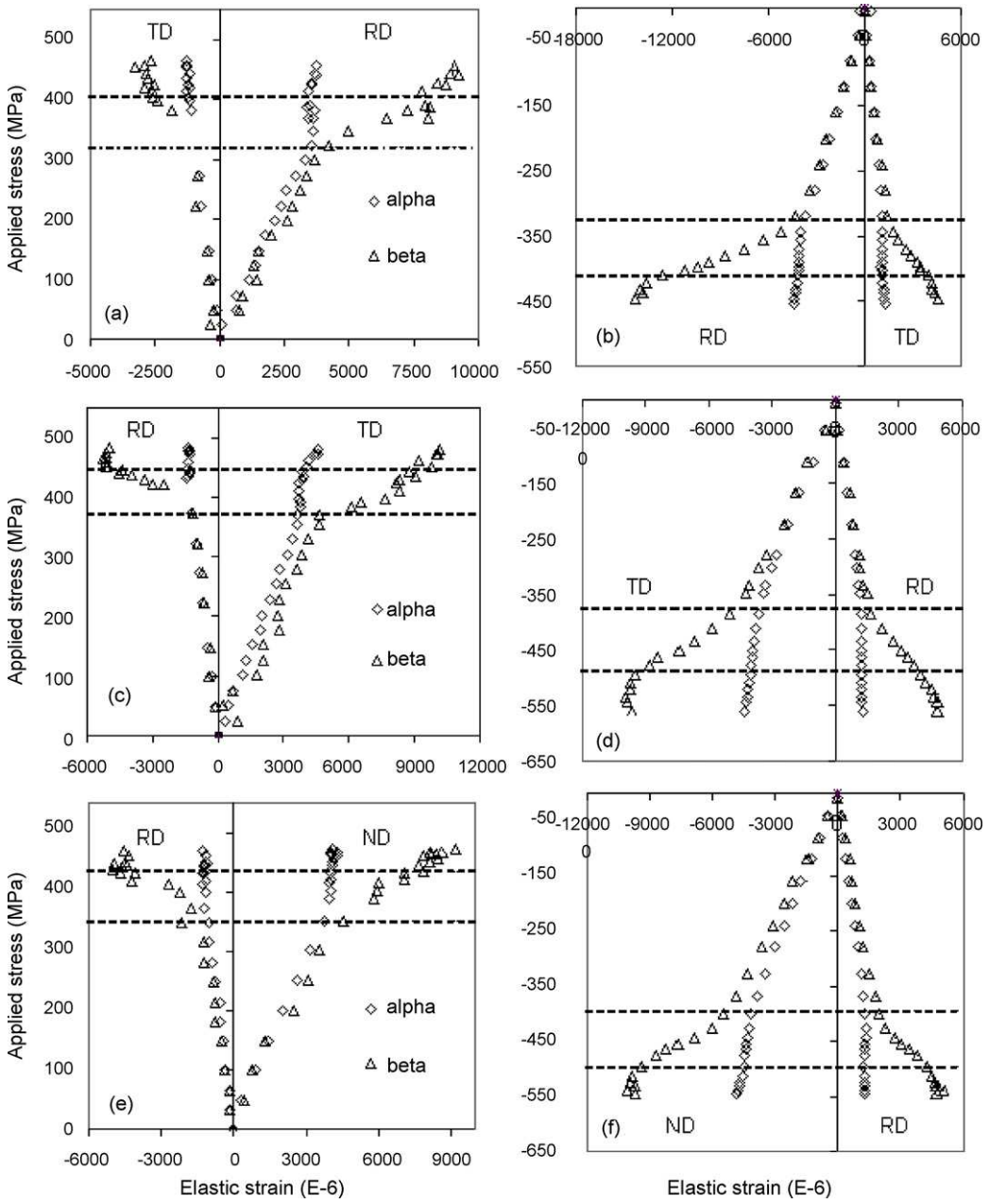

Fig. 4. Phase response during tension (left) (a) RD/TD, (c) TD/RD, (e) ND/RD and compression (right) (b) RD/TD, (d) TD/RD, (f) ND/RD. For tension data, the errors are ∼(100–200) × 10^{-6} for the α-phase and ∼(200–500) × 10^{-6} for the β-phase. For compression data, the errors are ∼(10–50) × 10^{-6} for the α-phase and ∼(50–200) × 10^{-6} for the β-phase. Dashed lines correspond to the yield of the α- and β-phases.

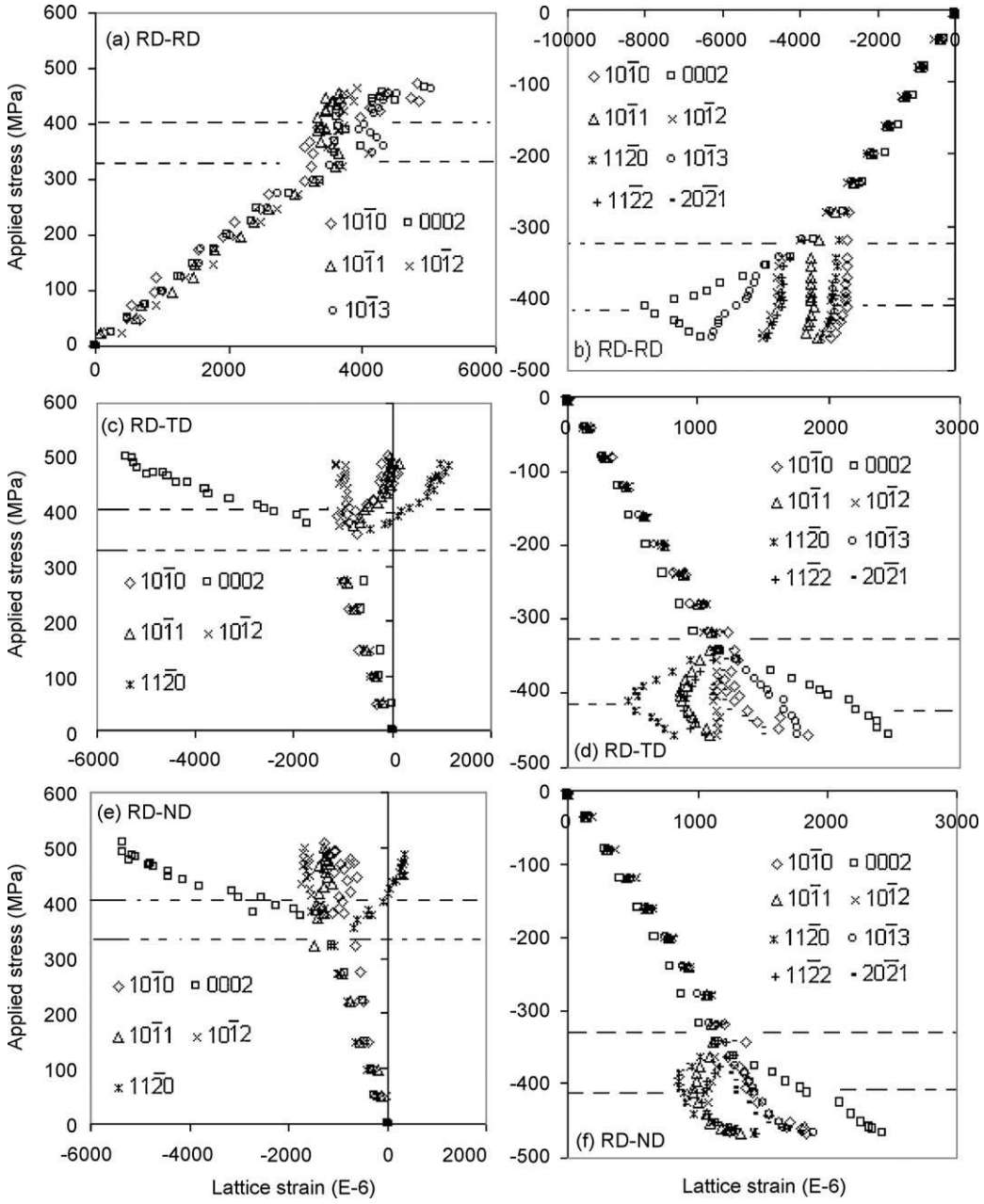

Fig. 5. Responses of individual grain orientations in the α-phase of RD samples during tension (left) and compression (right). Fig. 5(a) and (b) shows the results along the loading direction, the others show the results along the other two transverse directions. The errors are ~(100–200) × 10^{-6} for tension and ~(10–100) × 10^{-6} for compression. Dashed lines correspond to the yield of the α- and β-phases.

sonably accurate results in a relatively shorter data collection time compared to that needed for strain measurement of individual grain families. This is especially useful in determining the average phase response of the β_{Zr} in Zr–2.5Nb. Since the volume fraction of the β_{Zr} in Zr–2.5Nb is very small, the diffraction peaks are very weak, thus the peak average method [32] was found to be impracticable for analysis of the β_{Zr} in Zr–2.5Nb. For the *bcc* β-phase, the average phase strain was obtained directly from the lattice strain, while for the *hcp* α-phase, the average phase strain was calculated by:

$$\varepsilon_{ave} = f\varepsilon_c + (1-f)\varepsilon_a \quad (1)$$

where ε_c and ε_a are the lattice strains of ⟨*c*⟩ and ⟨*a*⟩ axes respectively, f is the resolved fraction of basal plane normals in the direction of interest [7], which is equivalent to the weighting approach discussed in [32]. For a random or weak texture, this simplifies to $(2\varepsilon_a + \varepsilon_c)/3$ [34]. Rietveld refinement was performed using the GSAS code [35]. The strains reported here are relative to the initial state, and thus do not take into account any initially existing residual stresses.

3. Experimental results

3.1. Macroscopic mechanical response

Macroscopic mechanical responses during tension and compression are shown in Fig. 3. The average Young's moduli and yield strengths (0.2%) in the three plate directions are listed in Table 1.

Observations can be summarized as:

(a) All of the three samples have a similar Young's modulus ~90–100 GPa during tension and compression.
(b) An obvious strength differential (SD) between tension and compression can be seen in Fig. 3. The yield strength of the TD and ND samples are higher in compression than in tension, while the strength in the RD is very close in tension and compression.
(c) The texture dependence of strength is weaker in tension than in compression, i.e. the strength differential in the three plate directions is much smaller in tension than that observed in compression. In compression, the TD and ND, which have the larger portion of ⟨c⟩ axis, have higher yield strengths ($\sigma_{0.2}$ = ~420 MPa) than RD (~350 MPa), while in tension all the three directions have a similar yield strength (~370–395 MPa).
(d) The elasto-plastic transition is gradual and smooth during compression, while this transition period is much shorter and sharper during tensile testing.

3.2. Average phase response

Fig. 4 shows the evolution of average phase elastic strains during tension and compression along the three principle plate directions, as determined by neutron diffraction. For reasons of space, each plot only shows the responses along the axial loading direction and the results along one of the two Poisson's directions. Qualitatively similar behavior is obtained in the other Poisson's direction. Only the elastic strains relative to the starting point are plotted in Fig. 4, thus showing the development of internal strains caused by deformation. In both tension and compression, the elastic anisotropy is very small in all the three plate directions. The Young's modulus of

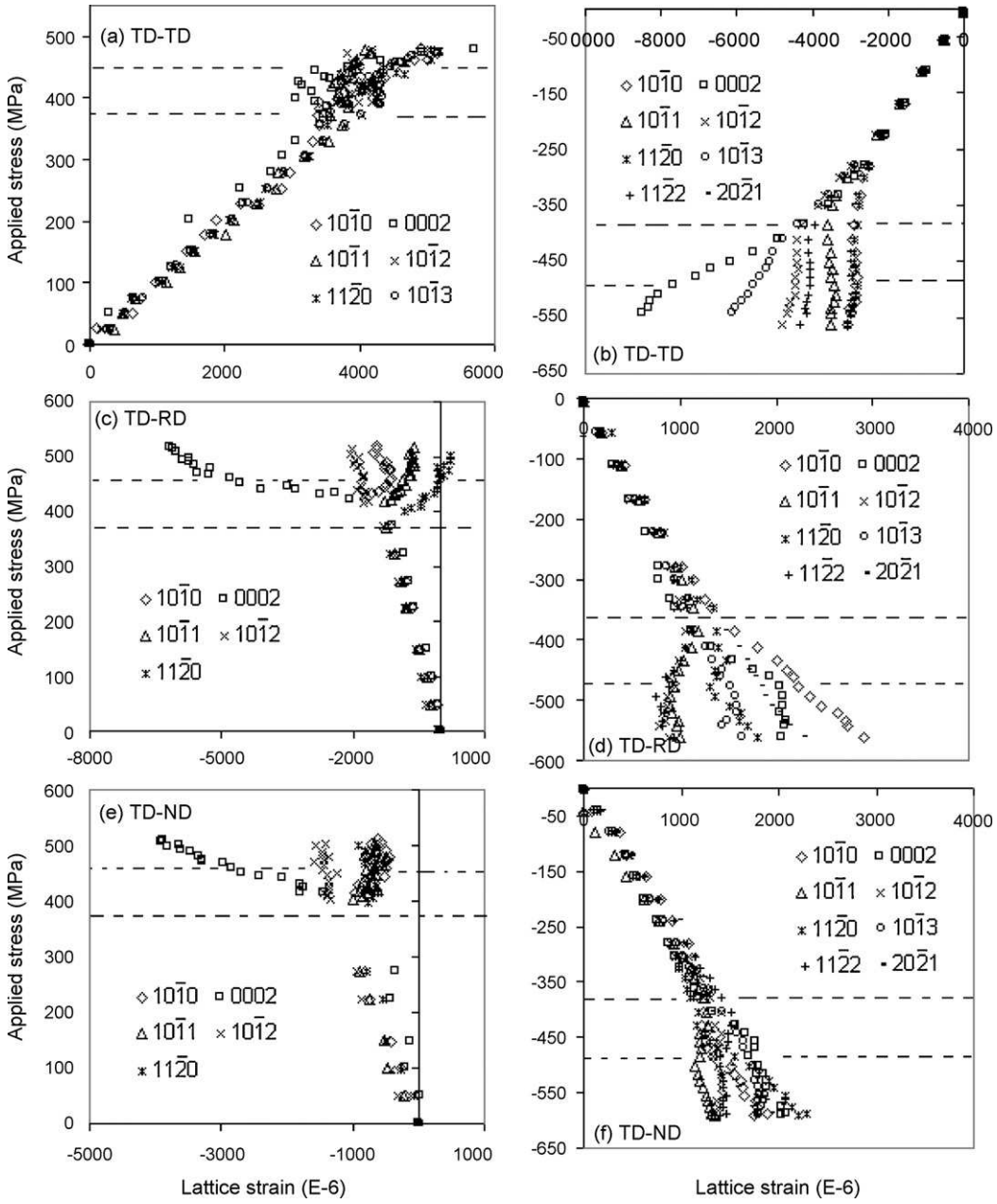

Fig. 6. Responses of individual grain orientations in the α-phase of TD samples during tension (left) and compression (right). Dashed lines represent the yield of the α- and β-phases.

the β-phase is smaller than that of the α-phase, hence more stress is taken up by the α-phase in the elastic region, which may cause it to yield at lower applied stress than it would without the β-phase present. The yield point of the α-phase is represented by the first inflection point in the stress–strain curve and is indicated by the dashed lines in Fig. 4a. It is seen that during tension in RD the α-phase yields at an applied stress ~320 MPa, which is close to the yield strength of the RD sample. Once the α-phase yields, its elastic stress–strain curve shifts towards compression relative to its linear elastic response, while the elastic strain of the β-phase shifts to the opposite direction, indicating that with increasing applied stress, more and more stress is taken by the β-phase, i.e. there is a load transfer from the α-phase to the β-phase. The β-phase finally yields at an applied stress of about 400 MPa showing a second inflection in the stress–strain curve. More stress is then shared by the α-phase whose lattice strain shifts back towards tension. The transverse data show a qualitatively similar trend. Similar load partitioning between the α- and β-phases during tension is observed in other samples (Fig. 4c and e) and during compression (Fig. 4b, d and f).

3.3. Response of individual grain orientations

3.3.1. Evolution of intergranular strains in the α-phase

The evolution of intergranular strains in the α-phase during tension and compression is plotted in Figs. 5–7. The lines all start from zero strain, thus thermal residual strains are excluded and figures only show the evolution of lattice strains caused by deformation,

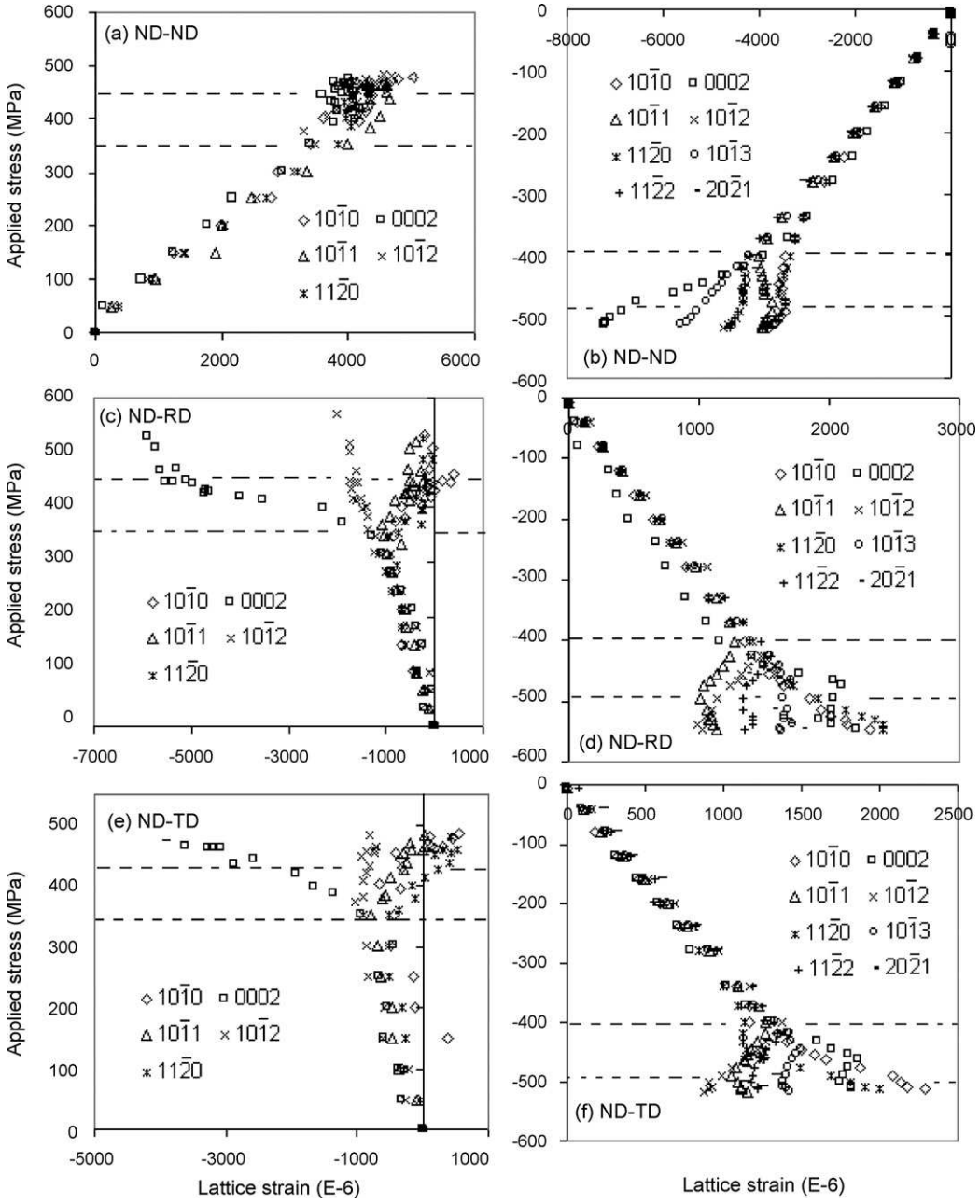

Fig. 7. Responses of individual grain orientations in the α-phase of ND samples during tension (left) and compression (right). Dashed lines represent the yield of the α- and β-phases.

relative to the starting state. Only selected stress–strain curves for individual grain families are plotted due to space limitations. The observations can be summarized as:

(a) In the elastic regime, there is a small level of elastic anisotropy during tension and compression along all the loading and transverse directions, however, an obvious plastic anisotropy is observed once plastic deformation occurs.
(b) During tension, the α-phase shows a small plastic anisotropy in the axial direction (Figs. 5a, 6a, 7a) but a larger plastic anisotropy in the Poisson directions (Figs. 5c, 5e, 6c, 6e, 7c, 7e). However during compression the α-phase exhibits a large plastic anisotropy in the loading direction (Figs. 5b, 6b, 7b) but a relatively small plastic anisotropy in the Poisson directions (Figs. 5d, 5f, 6d, 6f, 7d, 7f). This feature is perhaps more clearly seen in Fig. 8, where the lattice strain is plotted instead against the macroscopic true strain to highlight the strain anisotropy in the plastic region. Similar behavior has been observed in single phase Zircaloy-2 [36–38].
(c) During compression along the axial direction, the $\{1\,0\,\bar{1}\,0\}$ grain family yields first, defined as the first inflection of its stress–strain curve, at a lattice strain about 3000×10^{-6} and its stress–strain curve shifts backwards relative to its elastic line. Load is transferred to other orientations whose lattice strains thus increase by larger steps for a given applied stress increment; the $\langle 0\,0\,0\,2\rangle$ is the plastically hardest orientation and thus

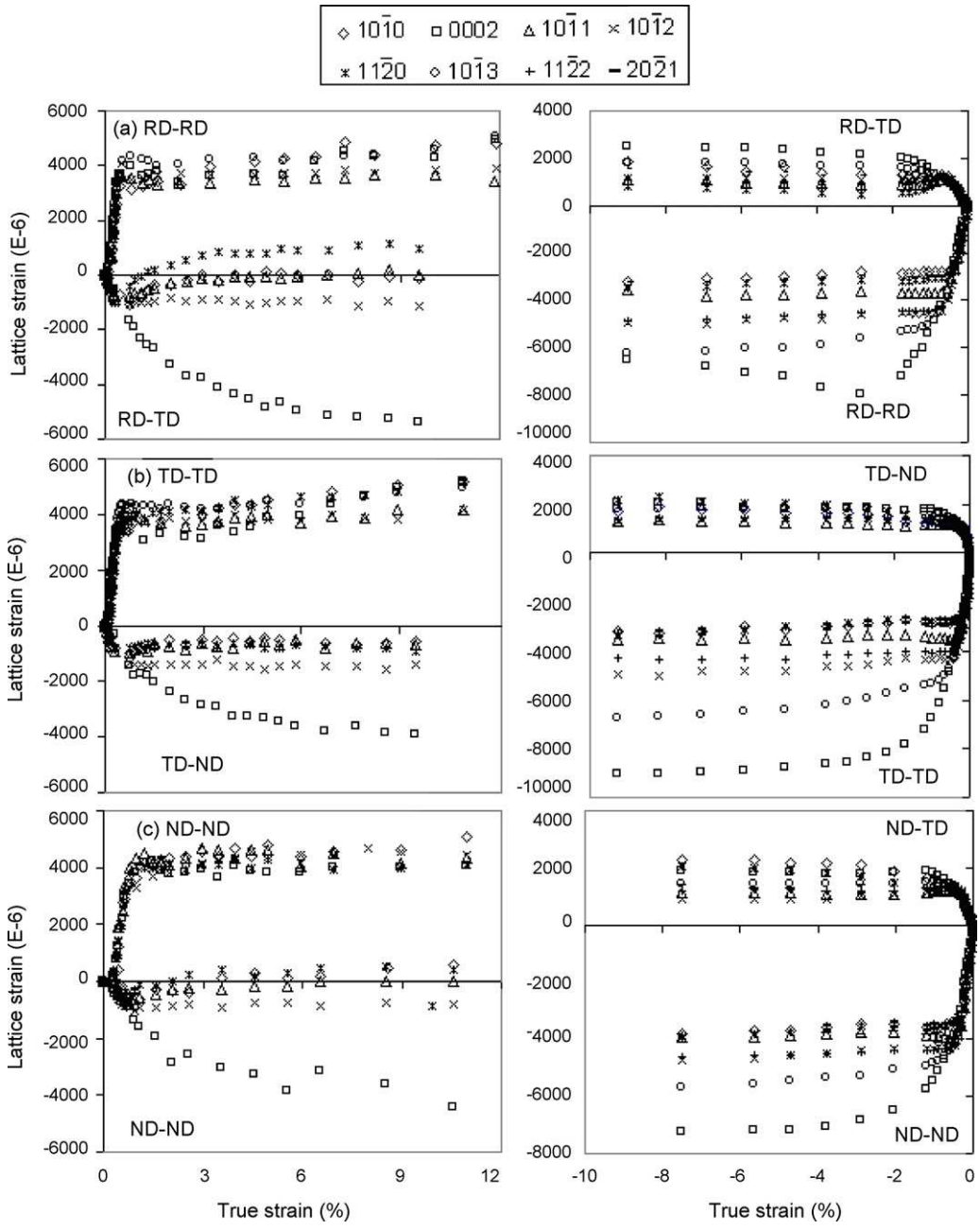

Fig. 8. Lattice strain plotted against macroscopic true strain during tension (left) and compression (right) for the α-phase diffraction peaks. (a) Tests along RD; (b) tests along TD; (c) tests along ND. Diffraction data from only one transverse direction is shown.

yields last at a lattice strain of about 8000×10^{-6}. In between the yield of the $\{1\,0\,\bar{1}\,0\}$ and the $\{0\,0\,0\,2\}$ grain families, the $\{1\,0\,\bar{1}\,1\}$, $\{1\,0\,\bar{1}\,2\}$ and $\{1\,0\,\bar{1}\,3\}$ grain families yield as the applied load progressively increases. For grain families such as $\{1\,0\,\bar{1}\,1\}$, $\{1\,0\,\bar{1}\,2\}$, $\{1\,0\,\bar{1}\,3\}$ and $\{0\,0\,0\,2\}$, the designation of 'yield' is based on the observation of strains parallel to the applied load curving back towards their elastic lines.

(d) This sequence in yielding is not really observable during tension tests (e.g. Fig. 6a). All the selected grain orientations yield at a similar lattice strain level ($\sim(3000–4000) \times 10^{-6}$). The $\{1\,0\,\bar{1}\,3\}$ grain family appears to actually be the last one to yield.

3.3.2. Evolution of intergranular strains in the β-phase

The evolution of lattice strains of the β-grains along the loading direction is plotted in Fig. 9. Generally, the tension and compression directions show a similar mechanical behavior, i.e. a small elastic anisotropy in the elastic region and an obvious plastic anisotropy in the plastic regime. In the elastic region, the $\{2\,0\,0\}$ has a smaller elastic modulus while $\{1\,1\,0\}$ and $\{2\,1\,1\}$ have the same value as each other. It is also shown that the elastic anisotropy in ND is larger than that in the other two plate directions. In the plastic region, the strains of the β-grains are strongly affected by the response of the α-phase, i.e. the lattice strains of all the selected orientations of the β-phase increase at larger steps once $\{1\,0\,\bar{1}\,0\}$ grain family of the α-phase yields. These grains thus take more and more stresses from the α-phase as the strain increases, and finally yield at a stress close to the yield point of the $\{0\,0\,0\,2\}$ grain family of the α-phase. Among the selected grain orientations, $\{2\,0\,0\}$ is the last one to yield. Compared with the α-phase, the deformation of the β-phase is more symmetric. All the selected grain orien-

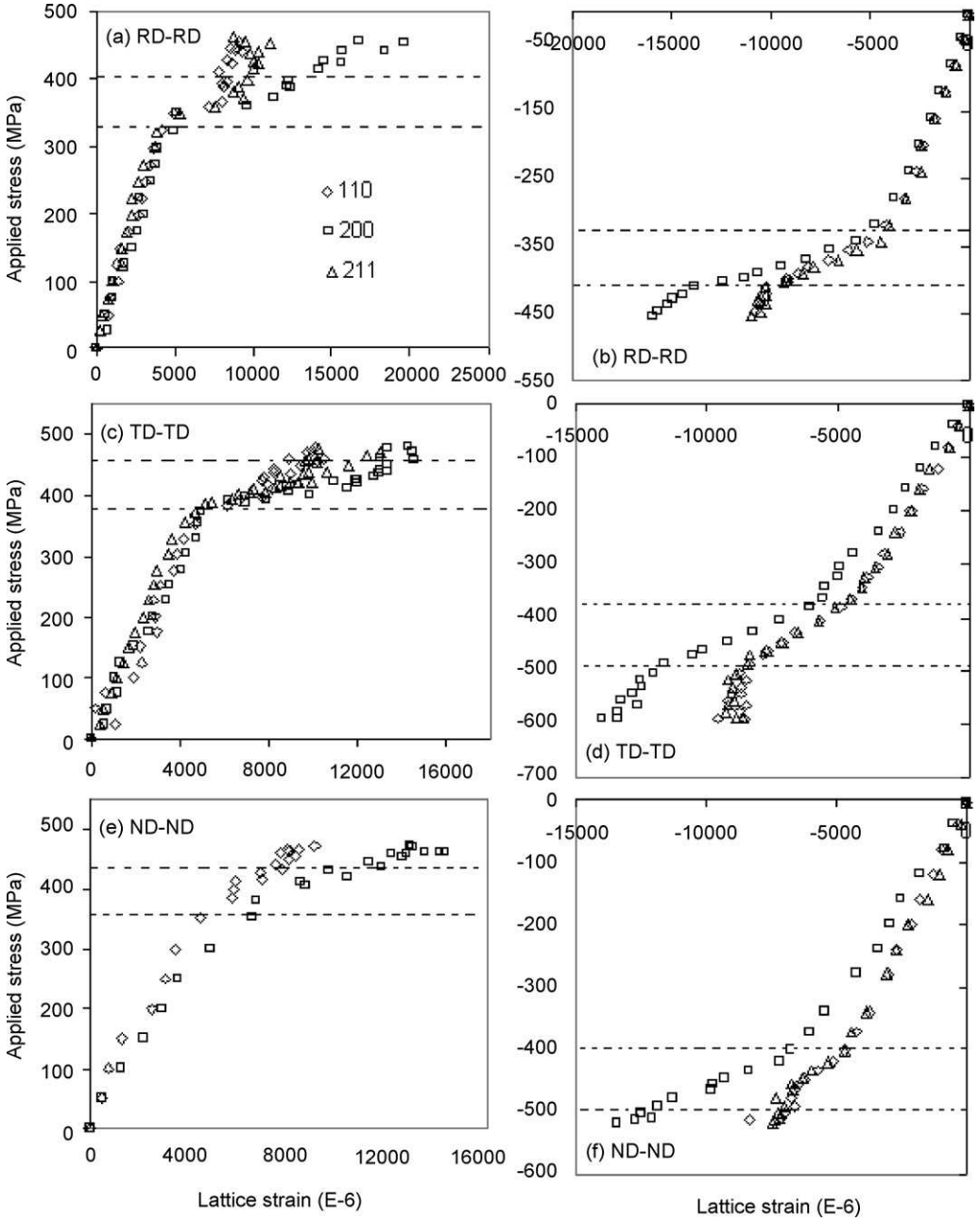

Fig. 9. Responses of individual grain orientations of the β-phase along three plate directions during tension (left) and compression (right). The uncertainty is $\sim(200–500) \times 10^{-6}$ for tension and $\sim(50–300) \times 10^{-6}$ for compression. Dashed lines represent the yield of the α- and β-phases.

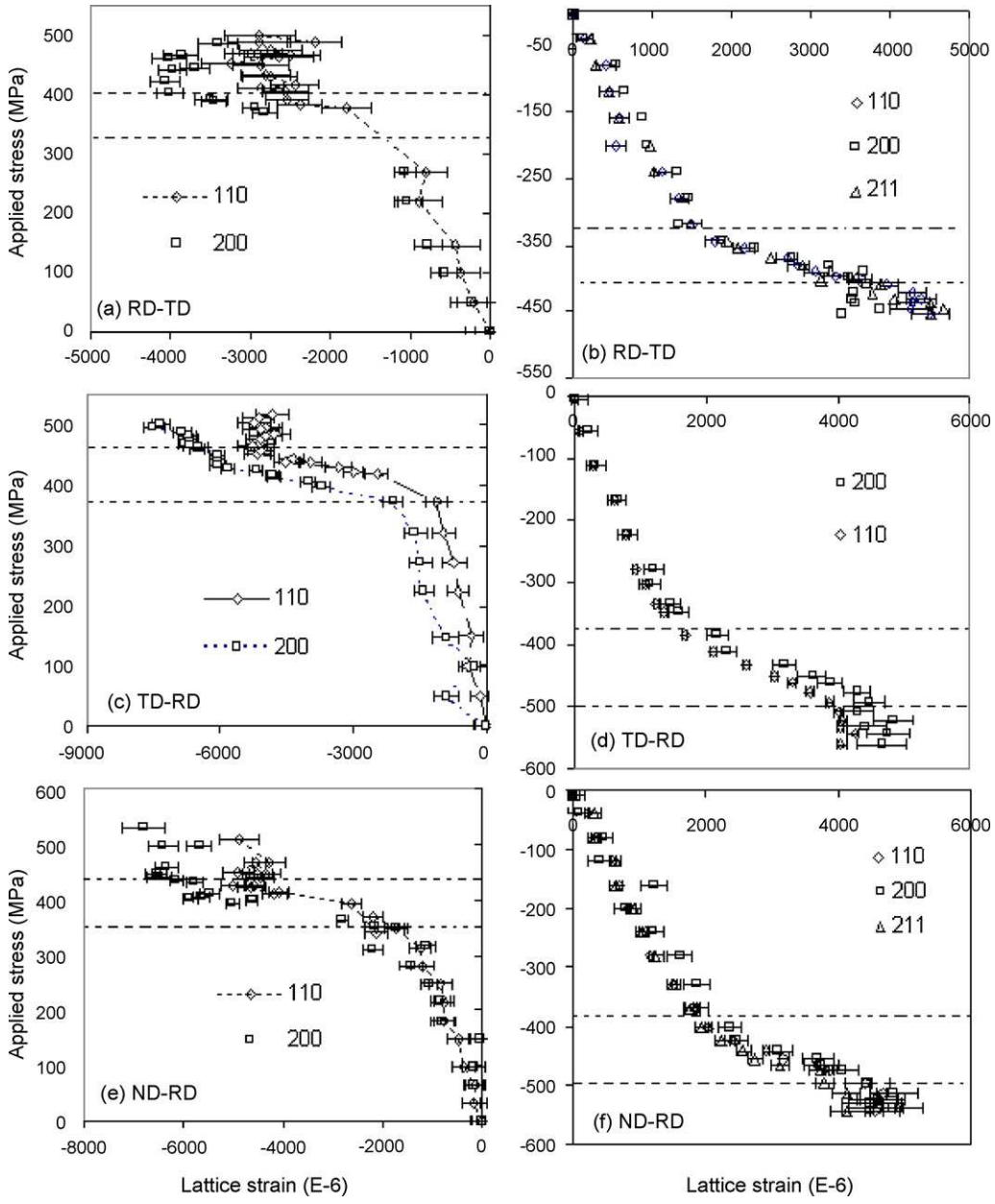

Fig. 10. Poisson strains of individual grain orientations of the β-phase during tension (left) and compression (right). Dashed lines represent the yield of the α- and β-phases.

tations yield at a similar lattice strain level during tension and compression. The {1 1 0} and {2 1 1} both yield at lattice strain ~10,000 × 10^{-6} during tension and compression, while {2 0 0} yields at lattice strain ~15,000 × 10^{-6} during both tension and compression.

Similar strain development of the β-grain families can be seen in the Poisson direction (Fig. 10). However, in the plastic region, the intergranular Poisson's strains (e.g. the strain difference between {2 0 0} and {1 1 0} grain families) are much smaller compared to the axial intergranular strains.

4. Discussion

Slight differences were observed in the pole figures of the initial (pre-deformation) material measured at HIPPO and Chalk River. This may be due to the fact that they were generated by the different techniques that are used for texture measurement at these two different types of facility. It is also possibly due to texture variation in the plate caused by inhomogeneities in the hot rolling process. The specified rolling temperature is ~700 °C, which is slightly above the monotectoid temperature of this material. During hot rolling, the front part of the plate would be in the α_{Zr} and β_{Zr} two phase region; some of the deformed β-phase then transforms to the α-phase after cooling to room temperature, which produced the {0 0 0 2} intensity in RD based on the Burger's relationship [39] (see Fig. 2). However, if the temperature dropped quickly during hot rolling, the back of the plate would then be rolled at temperatures just below the monotectoid temperature. Texture would then be determined by the combination of rolling strain and active deformation modes. Thus a lower {0 0 0 2} intensity in RD would be expected from the phase transformation after cooling. Since the texture of each sample was not measured before deformation, the exact start-

ing texture of each sample is not known. However the texture of each sample after deformation has been measured, and can be used, to some extent, to extrapolate the initial sample texture. Further, since this experiment and the discussion below focuses mostly on relative intensity changes for a given sample during the *in situ* deformation – which can be determined directly from the measured diffraction spectra – any small texture variations between samples should not cause significant trouble in interpretation of experimental data in terms of active deformation modes, although absolute starting intensities may vary slightly from sample to sample.

The similar Young's modulus obtained in the three plate directions indicate a weak texture dependence of elastic stiffness, which can be attributed to a combination of the weak texture and the strong constraints both between the α- and β-phases and among individual grains.

Fig. 3 shows that the strength differential between the tension and compression is largest in TD and smallest in RD, which have the highest and lowest basal plane normal concentrations respectively, indicating that this strength differential is primarily determined by the distribution of the ⟨*c*⟩ axes. As explained in [21,24], since both pyramidal ⟨*c*+*a*⟩ slip and twinning are much more difficult to activate than other slip systems and the *c*-axis of the α-Zr in this material is mostly concentrated along the TD and ND, higher strengths are expected along these two directions. However, the different texture dependence of strength during tension and compression implies that other factors such as the grain shape, the thermal residual stresses and/or twinning may take part of the responsibility for the strength anisotropy and the strength differential observed between tension and compression. Thermal residual stresses have been shown to cause the strength difference in tension and compression in single phase Zircaloy [40–42]. Twinning is another potential source for the strength asymmetry due to the strength difference between tensile and compressive twinning, and/or between twinning and dislocation slip [24,37,38]. Lowden and Hutchinson have observed a similar strength asymmetry in Ti–6Al–4V [43] and they claimed that the strength differential is in fact caused by the different hydrostatic level and the sense of shear between tension and compression that is experienced by dislocations, leading to $\langle 1\,1\,\bar{2}\,3\rangle\ \langle c+a\rangle$ slip being easier in tension than in compression, and hence a higher yield strength in compression. The possible contributions and their influence in this material will be discussed later.

Contrary to [15–17], where in the explanation of texture development during cold rolling the α-grains are treated as rigid bodies during deformation and the accommodation of plastic strain is mainly by the β-phase, the phase strains shown in Fig. 4 give direct evidence that in this material the α-phase yields at a lower applied stress during room temperature deformation than does the β-phase. From Fig. 4, it can be seen that the lattice strain at yield is about 4000×10^{-6} for the α-phase and about 8000×10^{-6} for the β-phase respectively. Provided the Young's modulus for the α- and β-phases are ~100 GPa and 60 GPa [44], the phase yield strengths are estimated as 400 MPa and 480 MPa respectively. Thus, despite the fact that the {0 0 0 2} grain family in the α-phase is the strongest among all the grain families in this dual phase system, the average β-phase is actually stronger than the α-phase. This brings the explanation proposed in [15–17] regarding

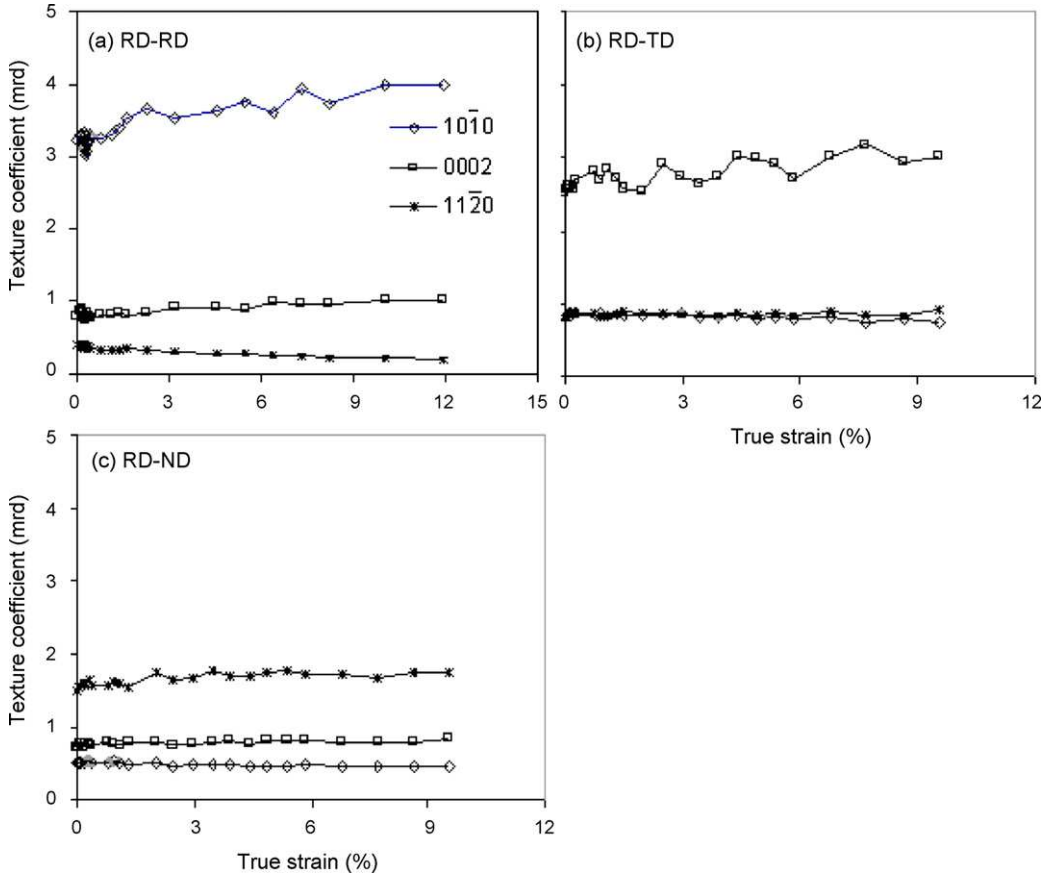

Fig. 11. Intensity change during tension of RD sample, (a) loading direction, (b) and (c) Poisson's directions. Errors are in the range of 3–16%.

the effect of the β-phase on the texture development in Zr–2.5Nb into question. The high strength of the β-phase could be due to its very fine grain size, and/or to preferential segregation of alloying elements. It is also in contrast to two phase titanium alloys such as Ti–6Al–4V, where the β-phase is usually considered to be softer.

Given that the single crystal elastic constants for $\langle 1\,0\,\bar{1}\,0\rangle$ and $\langle 0\,0\,0\,2\rangle$ crystal orientations are ~100 GPa and 125 GPa, the strains listed in Section 3.3.1 (c) roughly correspond to tensile yield stresses ~350 MPa and ~440 MPa and compressive yield stresses ~300 MPa and ~1000 MPa for $\{1\,0\,\bar{1}\,0\}$ and $\{0\,0\,0\,2\}$ grain families respectively, showing a significant asymmetrical yielding along the $\langle 0\,0\,0\,2\rangle$ orientation under tension and compression. This observation provides the explanation to the macroscopic behaviors described in Section 3.1. Since during compression, the $\{0\,0\,0\,2\}$ grain family can be seen to be plastically harder than other orientations (Figs. 5b, 6b, 7b), the yield stress of the material is mainly determined by the distribution of the $\langle c\rangle$ axis and thus shows a strong texture dependence. However, during tension all the grain orientations yield at a similar stress level (Figs. 5a, 6a, 7a), thus the material strength is less affected by the grain orientations, implying a small texture dependence of strength. All three samples have close yield strengths in tension and a similar short elasto-plastic transition period (Fig. 3a). The asymmetric yielding also causes different behaviors in the Poisson directions. Since the Poisson directions of a tensile loaded sample are under compression, the $\{0\,0\,0\,2\}$ grain family in the Poisson directions behaves much more strongly than other directions and causes a relative larger plastic anisotropy. Similarly, along the Poisson directions of a compression sample, all the grains have a similar strength and thus produce a relatively smaller plastic anisotropy compared to that in the loading direction.

5. Asymmetry of yielding

Two widely accepted sources for the asymmetric yielding in the α_{Zr} are thermal residual stresses [40–42] and twinning [24,37,38]. The α_{Zr} is thermally anisotropic with the thermal expansion coefficient of the $\langle c\rangle$ axis is $\sim 10.3\times10^{-6}\,K^{-1}$, almost double the value of the $\langle a\rangle$ axis, $\sim 5.8\times10^{-6}\,K^{-1}$ [45]. After cooling from the stress free temperature at ~900 K, the $\{1\,0\,\bar{1}\,0\}$ grain family will be under compression while the $\{0\,0\,0\,2\}$ grain family is under tension, thus the $\{1\,0\,\bar{1}\,0\}$ grain family will reach the yield surface at a higher applied stress in tension but a lower applied stress in compression, while the $\{0\,0\,0\,2\}$ grain family will be stronger in compression that in tension. Another potential contribution to asymmetric yielding is that due to the texture and the limited number of slip modes available, different deformation systems are activated during tension and compression [24,46]. $(1\,0\,\bar{1}\,2)\langle 1\,0\,\bar{1}\,1\rangle$ tensile twinning has been considered as easier than $\langle c+a\rangle$ pyramidal slip at room temperature and thus would occur when there is a tensile stress along the $\langle c\rangle$ axis or compression along the $\langle a\rangle$ axis [47]. Xu [38] showed that tensile twinning plays a major role in the deformation and texture evolution of textured Zircaloy-2. One interesting observation from [38] is the sharp "kick back" of the $\{0\,0\,0\,2\}$ grain family strain in the loading direction after compression along the directions with fewer basal plane normals. This strain "kick back" was attributed to tensile twinning in the Poisson's direction which

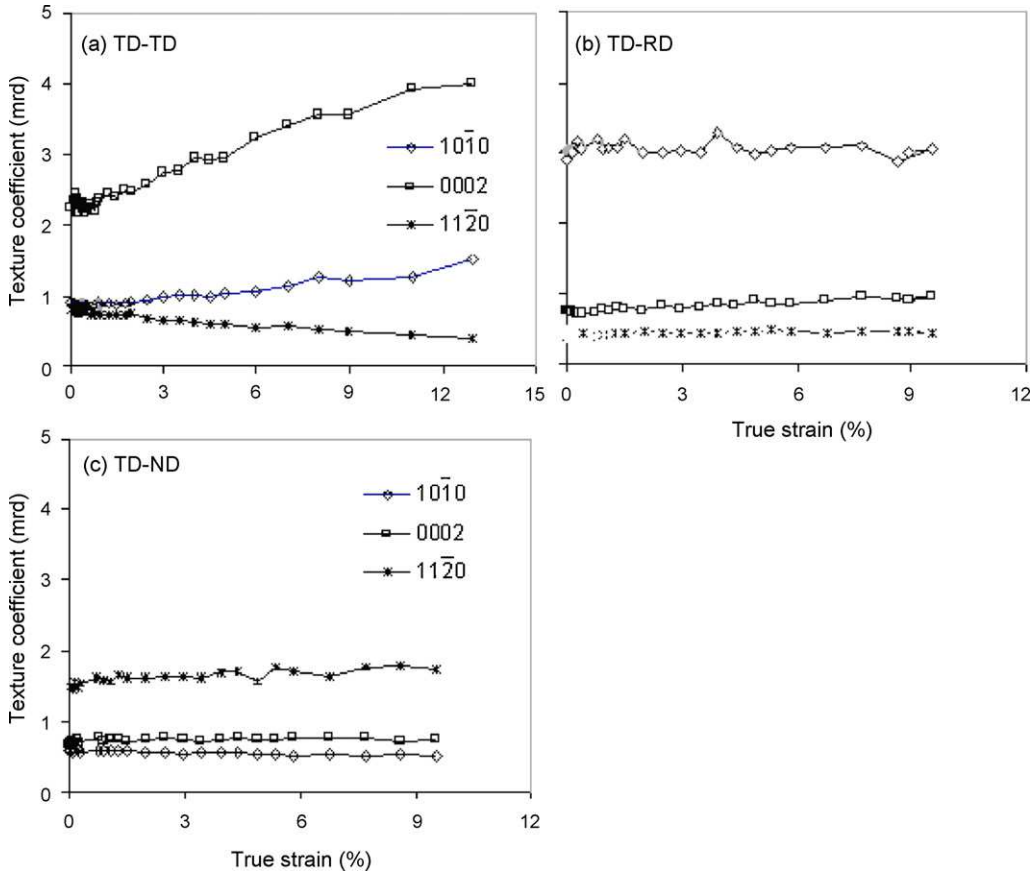

Fig. 12. Intensity change during tension of TD sample, (a) loading direction, (b) and (c) Poisson's directions. Errors are in the range of 3–14%.

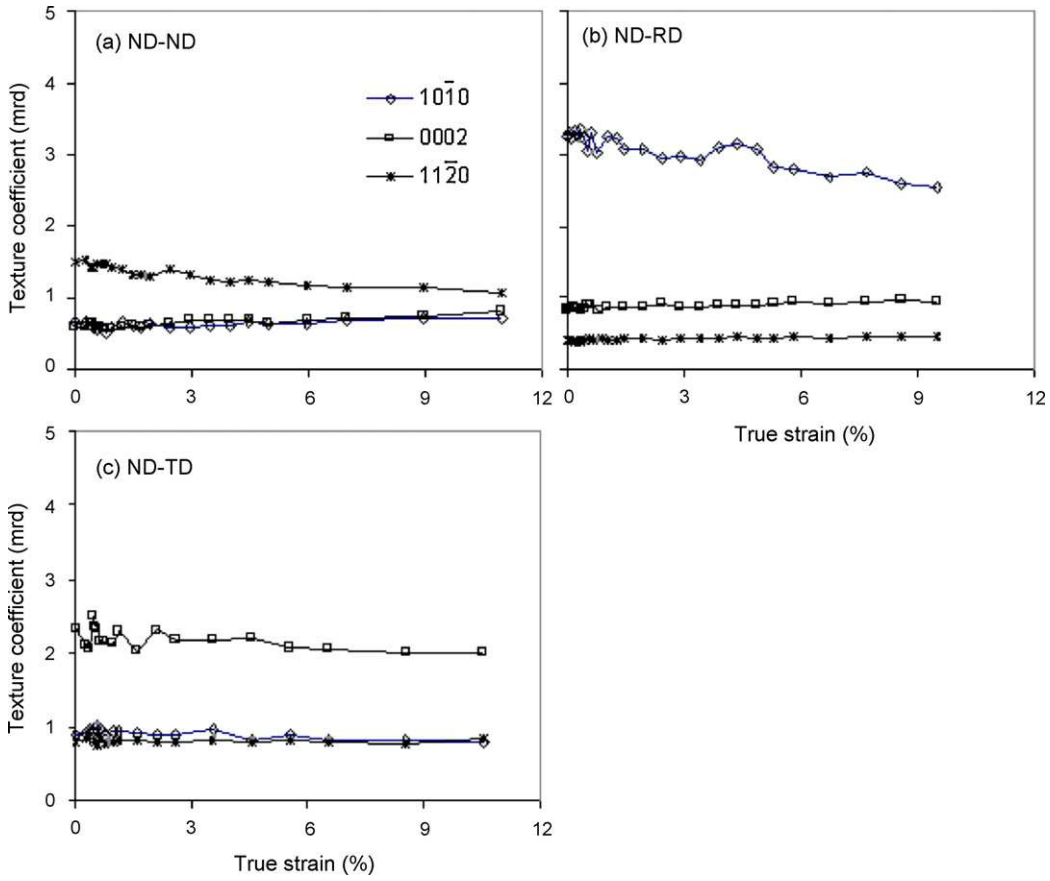

Fig. 13. Intensity change during tension of ND sample, (a) loading direction, (b) and (c) Poisson's directions. Errors are in the range of 4–10%.

rotated the crystal lattice and generated new {0002} grains in the axial compression direction to reduce the average axial {0002} strain. This explanation is supported by a large {0002} intensity increment in the loading direction with a corresponding intensity drop in the {0002} intensity in the Poisson's direction. A similar observation of a strain 'kick back' is obtained in the compressed RD sample here (see Fig. 5b), which may at first sight suggest the occurrence of tensile twinning in our material. $(10\bar{1}2)\langle 10\bar{1}1\rangle$ tensile twinning causes a ~90° rotation of the ⟨*c*⟩ axis and thus decreases the {0002} intensity in the tensile loading direction, which hence allows the confirmation of the presence of tensile twinning by analyzing the intensity change of the {0002} and $\{10\bar{1}0\}$ grain families in the two perpendicular detector banks. To verify whether or not tensile twinning is responsible for the relatively lower tensile strength of the {0002} grain family compared to its compressive strength, the evolution of peak intensities of the $\{10\bar{1}0\}$, {0002} and $\{10\bar{2}0\}$ grain families during tension along the three plate directions are plotted in Figs. 11–13. Due to the texture variation in the plate (i.e. texture may be slightly different in different samples), the relationship between measured diffraction peak intensity and texture coefficient for each sample was determined based on the measurement made on each sample after deformation. It can be seen that during tension the {0002} intensity increased rather than decreased in the tensile axis, especially in the tension TD (Fig. 12a), indicating that twinning is not the major deformation mode during tension along the ⟨*c*⟩ axis of this material. The {0002} intensity increase in the tensile loading direction is instead likely caused by pyramidal $\{10\bar{1}1\}\langle 11\bar{2}3\rangle$ slip [38].

The intensity change during compression along RD of the hot rolled Zr–2.5Nb plate is plotted in Fig. 14. It is shown that the {0002} intensity increased in the compressive loading direction and decreased in the Poisson's direction (e.g. TD), which might suggest that tensile twinning in the Poisson direction is responsible for the {0002} strain "kick back" in the compressed RD. However it can be seen that the initial {0002} intensity in RD is very weak, and the increment in intensity is very small compared to that observed by Xu [38], indicating that if tensile twinning has occurred, it only played a minor role in the deformation of this material. The small {0002} intensity increment in the compressed RD could also be explained by activity of basal ⟨*a*⟩ slip [38]. It is worth noting that the {0002} strain "kick back" observed in the compressed RD is also seen in tensile loading tests such as in the axial direction of the tensile loaded TD sample (Fig. 6a) and to a lesser extent in the RD sample (Fig. 5a), which are unlikely to have twinning occurring, as discussed before. In addition, despite extensive SEM and TEM investigation we were unable to find microscopic evidence of twinning. We conclude therefore that the {0002} strain "kick back" is more likely caused by other stress relaxation mechanisms which relate to the dislocation evolution occurring during deformation.

Based on the above discussions, it is evident that although twinning, as one of the important deformation modes in some Zr alloys, cannot be totally excluded from the results of this experiment, it is considered a minor deformation mode in this material and is unlikely to be responsible for the asymmetric yielding of the {0002} grain family between tension and compression.

Hutchinson and co-workers [43,48] have given another possible explanation for the asymmetry in deformation along the ⟨*c*⟩ axis. In their studies of textured Ti–6Al–4V alloys, they found that when compressed along the ⟨0002⟩ direction, the $\langle 11\bar{2}3\rangle$ dislocations

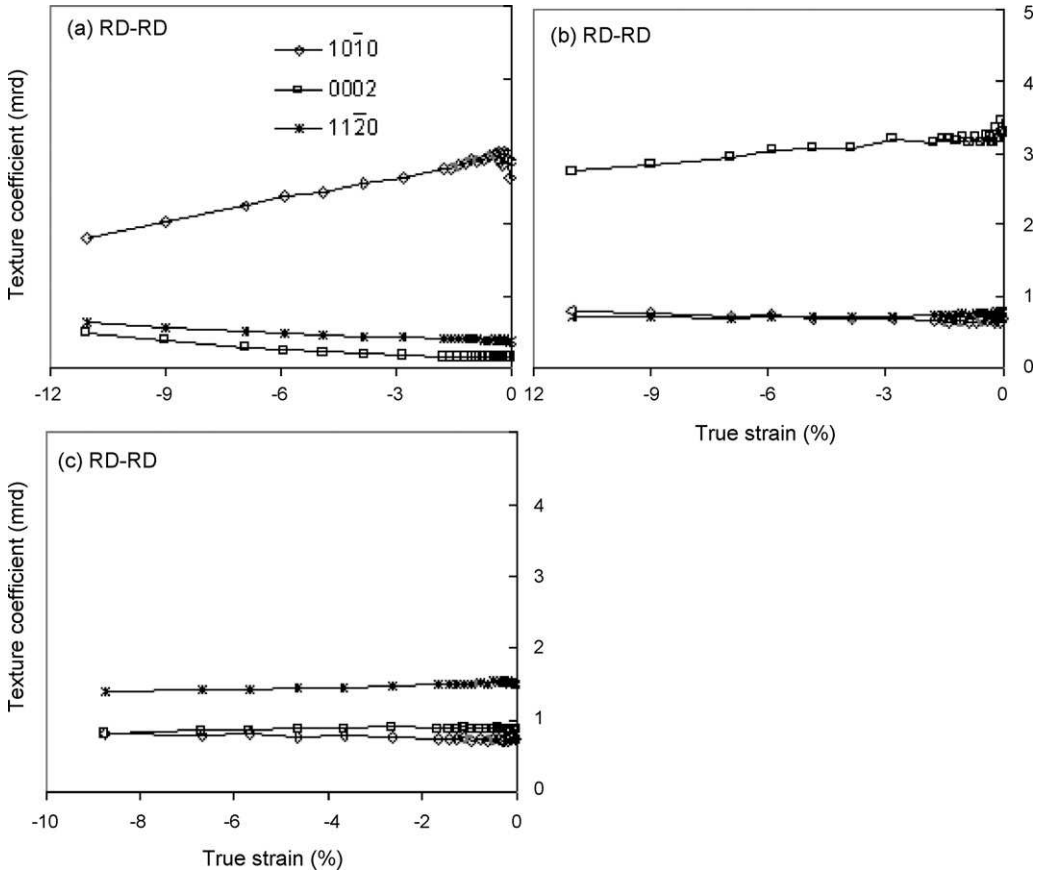

Fig. 14. Intensity change during compression of RD sample, (a) loading direction, (b) and (c) Poisson's directions. Errors are in the range of 1–6%.

move on the $\{1\,0\,\bar{1}\,1\}$ planes with considerable cross slip, but do not cross slip during tension. They attributed this to a higher CRSS for pyramidal $\langle c+a\rangle$ slip during compression than during tension. Associated with the dilatation normal to the slip plane and different directions of the dislocation movement during tension and compression, they proposed that the slip of $\langle 1\,1\,\bar{2}\,3\rangle$ $\langle c+a\rangle$ dislocation is dependent on the stress state and the shear direction, and it is easier in tension than in compression. Bearing in mind that Zr–2.5Nb has a similar microstructure and crystal structure to Ti–6Al–4V, it is reasonable to believe that Hutchinson's theory may also explain the asymmetric yielding observed in zirconium alloys, as pointed out by Christodoulou [49].

For the β-phase, the small elastic anisotropy in the RD and TD (Fig. 9a–d) implies a strong constraint along these two directions, while a relatively larger elastic anisotropy along the ND (Fig. 9f), indicates a relatively weak constraint in ND, which may be attributed to the character of the microstructure such as the grain shape, geometry and phase distribution. Since the $\{1\,1\,0\}$ and $\{2\,1\,1\}$ grain families have a larger elastic modulus than the $\{2\,0\,0\}$ grain family, they bear more stress in the elastic regime and thus yield at a lower applied stress even though they have a higher Taylor factor than $\{2\,0\,0\}$ for $(1\,1\,0)$ $\langle 1\,1\,1\rangle$ slip system. Similar observations in *bcc* ferrite have been explained by Oliver et al. [50].

Fig. 15 shows the changes in diffraction peak width observed in both phases during deformation, parallel to the loading direction. In contrast to Kumar et al. [17], where significant peak broadening was only observed in the β-phase peaks and not in the α-phase, peak broadening was seen in all diffraction peaks in both phases during deformation with broadening increasing with deformation strain. While there are many possible contributions to an increasing peak width, it seems likely that plastic strain is occurring in both phases, in contrast to Kumar's rigid α-phase model. In Kumar's study, X-ray diffraction was used, which limited the data acquisition to near the surface of the sample, and the comparison was made only between the $\{1\,0\,\bar{1}\,2\}$ α peak and the $\{2\,0\,0\}$ β peak which may have contributed to the observation. Fig. 15 also shows that in the α-phase there is a trend of peak broadening increasing with increasing $\langle c\rangle$ component during compression but that this trend is rather vague during tension. Similar phenomena were observed in the TD and ND samples. Peak broadening in the loading directions could be caused by heterogeneous dislocation distribution, strain distributions (i.e. strain varying with position), grain size and other instrumental factors [51]. If the effect of instrumental factors is unchanging during a test, and the strain distribution and grain size evolution can be assumed to be similar during tension and compression, then the asymmetric peak broadening shown in Fig. 15 may provide another evidence for asymmetric dislocation evolution during tension and compression.

From Fig. 4, it can be seen that the lattice strain of the β-phase at yield is about $(8000–10{,}000)\times 10^{-6}$. Assuming the Young's modulus is ~60 GPa [44], the yield strength of the β-phase in this material can be roughly estimated as ~500–600 MPa, which is comparable to the macroscopic yield strength obtained for the 100% β_{Zr} material in [44]. The high strength of the 100% β_{Zr} in [44] was attributed to the solution strengthening from the oxygen and niobium content, while the high β-phase strength in this hot rolled Zr–2.5Nb is likely caused by the strengthening of niobium content with a contribution from the small grain size.

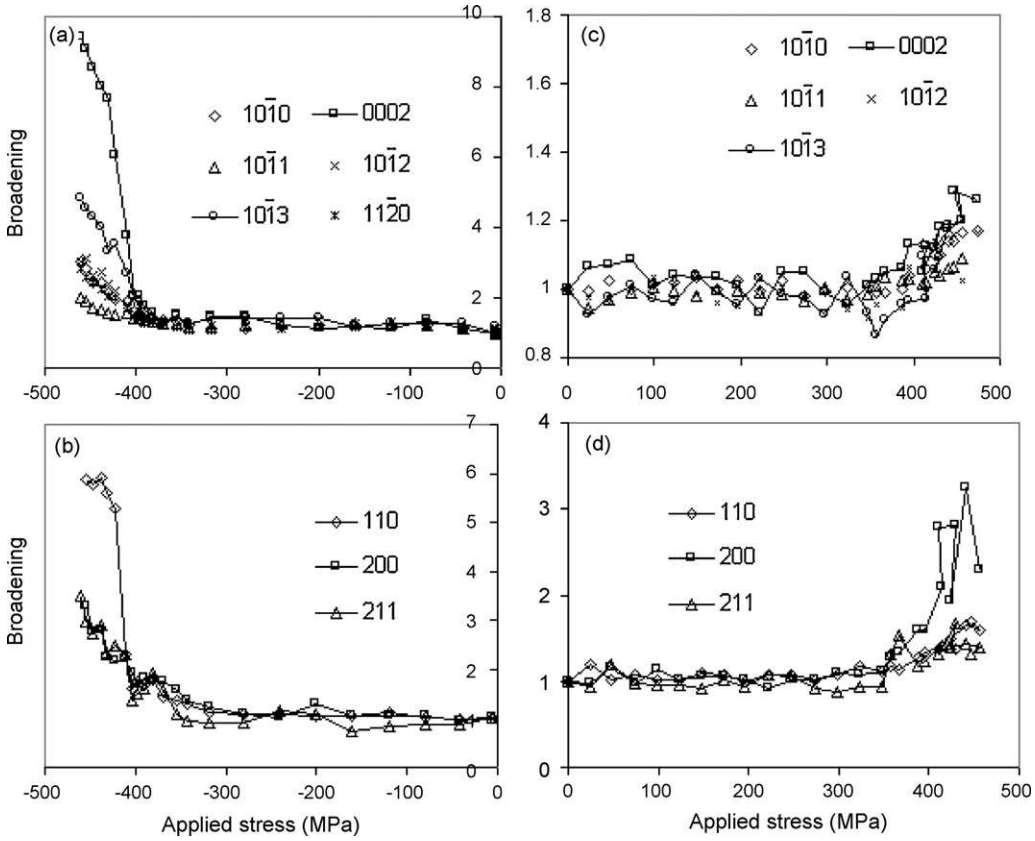

Fig. 15. Peak broadening in the loading direction of the RD sample, (a) α-grains, (b) β-grains during compression, (c) α-grains and (d) β-grains during tension. The uncertainty is less than 5% for alpha peaks and less than 10% for beta peaks.

6. Conclusions

Both *in situ* tension and compression tests have been carried out for textured Zr–2.5Nb plate material at room temperature. Deformation along all the three principle plate directions has been studied and the evolution of interphase and intergranular strains along all the loading and the Poisson's directions has been investigated through neutron diffraction. It is concluded that:

1. A strength differential and different texture dependence of strength was found during tension and compression. The influence of texture on strength is much larger in compression than in tension.
2. A significant asymmetric yielding of the {0 0 0 2} grain family is found during tension and compression, where the compression strength is much higher than the tensile strength. This causes the strength differential and different texture dependence of strength observed in this material.
3. The evolution of interphase and intergranular strain was determined by the relative phase properties, crystal properties and texture distribution. The average phase behaviors are similar during tension and compression, where the β-phase in this material is stronger than the α-phase. The asymmetric yielding of the {0 0 0 2} grain family results in a larger intergranular strain in the loading direction during compression than that obtained during tension.
4. The thermal residual stress and different CRSS for the $\langle c+a \rangle$ pyramidal slip during tension and compression are two possible reasons for this asymmetric yielding, and little evidence is found for twinning as contributing to this asymmetry.

Acknowledgements

The authors wish to acknowledge Drs. Igor Yakobtsov and Abdul Khan for TEM observations of this material, and Dr. Sven Vogel (Los Alamos National Lab.) for texture measurements on the material. This work is sponsored by NSERC, COG, OPG and Nu-Tech Precision Metals under the Industrial Research Chair Program in Nuclear Materials at Queen's University. Neutron diffraction experiments were carried out at the Los Alamos Neutron Scattering Center, Los Alamos National Laboratory, USA, the National Research Universal (NRU) reactor at the AECL Chalk River Laboratory (CRL), Canada and ISIS pulsed neutron facility, Rutherford Appleton Laboratory, UK.

References

[1] D.G. Hurst, Canada Enters the Nuclear Age, McGill-Queen's University press, 1997.
[2] R.A. Holt, N. Christodoulou, A.R. Causey, J. Mater. Nucl. 317 (2003) 256.
[3] N. Christodoulou, P.A. Turner, C.N. Tome, C.K. Chow, R.J. Klassen, Metall. Mater. Trans. A 33 (2002) 1103.
[4] C.N. Tome, N. Christodoulou, Philos. Mag. 80 (2000) 1407.
[5] E.E. Ibrahim, J. Nucl. Mater. 118 (1983) 260.
[6] R.A. Holt, J. Nucl. Mater. 159 (1988) 310.
[7] R.A. Holt, E.F. Ibrahim, Acta Metall. Mater 27 (1979) 1319.
[8] M. Griffiths, N. Christodoulou, S.A. Donohue, J. ASTM Int. (2005) 2.
[9] A.R. Causey, C.H. Woo, R.A. Holt, J. Nucl. Mater. 159 (1988) 225.
[10] R.A. Holt, J. Nucl. Mater. 90 (1980) 193.
[11] R.A. Holt, J. Nucl. Mater. 372 (2008) 182.
[12] R.A. Holt, S.A. Aldridge, J. Nucl. Mater. 135 (1985) 246.
[13] R.A. Holt, P. Zhao, J. Nucl. Mater. 335 (2004) 520.
[14] B.A. Cheadle, C.E. Ells, J. Electrochem. Technol. 4 (1966) 329.
[15] K. Kapoor, D. Lahiri, S.V.R. Rao, T. Sanyal, N. Saibaba, B.P. Kashyap, Mater. Sci. Technol. 20 (2004) 1281.
[16] M.K. Kumar, C. Vanitha, I. Samajdar, G.K. Dey, R. Tewari, D. Srivastava, S. Banerjee, J. Nucl. Mater. 335 (2004) 48.

[17] M.K. Kumar, I. Samajdar, N. Venkatramani, G.K. Dey, R. Tewari, D. Srivastava, S. Banerjee, Acta Mater. 51 (2003) 625.
[18] S. Cai, M.R. Daymond, R.A. Holt, E.C. Oliver, Adv. Mater. Res. 15–17 (2007) 615.
[19] A. Salinas-Rodriguez, Acta Metall. Mater. 43 (1995) 485.
[20] A. Salinas-Rodriguez, J.H. Root, Texture Microstruct. 14–18 (1991) 1239.
[21] B.A. Cheadle, C.E. Ells, W. Evans, J. Nucl. Mater. 23 (1967) 199.
[22] S. Kim, Metall. Mater. Trans. 37A (2006) 59.
[23] N. Christodoulou, P.A. Turner, E.T.C. Ho, C.K. Chow, M. Resta Levi, Metall. Mater. Trans. A 31A (2000) 409.
[24] Z.H.A. Kassam, Z. Wang, E.T.C. Ho, Mater. Sci. Eng. 158 (1992) 185.
[25] P. Gangli, J. Root, R. Fong, Can. Metall. Q 34 (1995) 211.
[26] R.A. Lebensohn, C.N. Tome, Acta Metall. Mater. 41 (1993) 2611.
[27] D.X. Du, C.H. Woo, Comput. Mater. Sci. 23 (2002) 260.
[28] R. Choubey, S.A. Aldridge, J.R. Theaker, C.D. Cann, C.E. Coleman, Proceedings of the 11th International Symposium on Zirconium in the Nuclear Industry ASTM STP, vol. 1295, 1996, p. 657.
[29] R.B. Von Dreele, J. Appl. Crystallogr. 30 (1997) 517.
[30] M.R. Daymond, H.G. Priesmeyer, Acta Mater. 50 (2002) 1613.
[31] J.R. Santisteban, M.R. Daymond, L. Edwards, J.A. James, J. Appl. Crystallogr. 39 (2006) 812.
[32] M.R. Daymond, J. Appl. Phys. 96 (2004) 4263.
[33] M.R. Daymond, M.A.M. Bourke, R.B. Von Dreele, B. Clausen, T. Lorentzen, J. Appl. Phys. 82 (1997) 1554.
[34] M.R. Daymond, M.A.M. Bourke, R.B. Von Dreele, J. Appl. Phys. 85 (1999) 739.
[35] A.C. Larson, R.B. Von Dreele, Report No. LAUR 86-748, Los Alamos National Laboratory, 1994.
[36] J.W.L. Pang, T.M. Holden, P.A. Turner, T.E. Mason, Acta Mater. 47 (1999) 373.
[37] E.C. Oliver, M.R. Daymond, P.J. Withers, Mater. Sci. Forum 495–497 (2005) 1553.
[38] F. Xu, Ph.D. Thesis, Queen's University, 2007.
[39] W.G. Burger, Physica 1 (1938) 561.
[40] S.R. MacEwen, C. Tome, J. Faber, Acta Metall. 37 (1989) 979.
[41] P.A. Turner, C.N. Tome, Acta Metal. Mater. 42 (1994) 4143.
[42] P.A. Turner, N. Christodoulou, C.N. Tome, Int. J. Plast. 11 (1995) 251.
[43] M.A.W. Lowden, W.B. Hutchinson, Metall. Trans. 6 (1975) 441.
[44] S. Cai, M.R. Daymond, R.A. Holt, E.C. Oliver, J. Nucl. Mater., submitted for publication.
[45] C.N. Tomé, N. Christodoulou, P.A. Turner, M.A. Miller, C.H. Woo, J. Root, T.M. Holden, J. Nucl. Mater. 227 (1996) 237.
[46] S.R. MacEwen, C.E. Ells, O.T. Woo, J. Nucl. Mater. 101 (1981) 336.
[47] C.N. Tome, P.J. Maudlin, R.A. Lebensohn, G.C. Kaschner, Acta Mater. 49 (2001) 3085.
[48] I.P. Jones, W.B. Hutchinson, Acta Metall. 29 (1981) 951.
[49] N. Christodoulou, Acta Metall. 37 (1989) 529.
[50] E.C. Oliver, M.R. Daymond, P.J. Withers, Acta Mater. 52 (2004) 1937.
[51] B.D. Cullity, Element of X-rays Diffraction, Second edition, Addison-Wesley Publishing Company, Inc., 1978.